Millimeter-Wave Thin Lens Using Multi-Patch Incorporated Unit Cells for Polarization-Dependent Beam Shaping

INSEOP YOON[1], (Student Member, IEEE), AND JUNGSUEK OH[2,3], (Senior Member, IEEE)

[1]Department of Electronic Engineering, Inha University, Incheon 22212, South Korea
[2]Institute of New Media and Communications, Seoul National University, Seoul 08826, South Korea
[3]School of Electrical and Computer Engineering, Seoul National University, Seoul 08826, South Korea

Corresponding author: Jungsuek Oh (jungsuek@snu.ac.kr)

ABSTRACT This paper describes a millimeter-wave thin lens that exhibits different beam-shaping characteristics depending on the polarization of the incident waves. The proposed unit cell topologies, which use multiple rectangular patches and rectangular-slotted grids, enable thinner ($= 0.05\lambda_0$) and smaller ($= 0.168\lambda_0$) features than in previous polarization-dependent lenses. An appropriate set of the proposed unit cells is shown to cover a tunable phase range of 180° with respect to one polarized wave but have an almost-zero tunable range of phase shifts with respect to another polarized wave. Thus, using this unit cell set for x-polarized incident waves, the proposed lens operates as a convex lens, whereas for y-polarized incident waves, the lens operates as a frequency selective surface. This confirms that gain variations of 13 dB or more can be differentiated according to the polarization of the incident waves on the lens, supporting polarization-dependent beam-shaping capability as a function of the polarization of incident waves.

INDEX TERMS Lens, metasurface, millimeter-wave antenna, polarization, spatial filter, transmit array.

I. INTRODUCTION

Mobile communication systems are expected to undergo an explosive increase in data usage because of the continuous growth in data traffic inspired by next-generation services such as the Internet of Everything (IoE). Therefore, worldwide organizations have been actively studying the millimeter-wave band for use as the 5G frequency. One essential requirement for millimeter-wave wireless communication is high antenna gain to compensate for high signal attenuation in the wireless channel. To achieve this, millimeter-wave thin lens technology, which consists of an array of sub-wavelength spatial filters, has received considerable attention as a novel way to boost antenna performance. The main approaches for improving antenna gain have focused on transforming spherical waves into plane waves. In particular, some

low-profile and extremely compact lenses have the potential to be used in millimeter-wave applications [1]–[3].

Recent design techniques for frequency selective surfaces (FSS) can synthesize accurate spatial filter responses owing to their relatively large degree of design freedom in controlling the profile of the electromagnetic waves [4]. Furthermore, it has been discovered that a wider range of phase shifts can be acquired by increasing the order of the filter response produced by multi-layer FSS. These multi-layer FSS can be bandpass or low-pass unit cells, where the geometrical difference between the two is that the low-pass unit cells consist of only patches, whereas bandpass unit cells consist of both patches and grids.

Such millimeter-wave thin lenses have mainly been studied in terms of improving antenna gain by transforming spherical waves into plane waves. Interestingly, most previous lens technologies utilizing the polarization characteristics of the incident waves have focused on transforming

The associate editor coordinating the review of this manuscript and approving it for publication was Yang Yang.
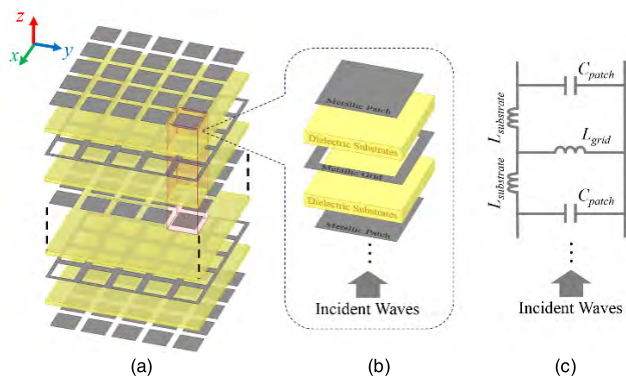
FIGURE 1. (a) Exploded view of a conventional thin lens, (b) exploded view of a unit cell (operating as a spatial filter), and (c) equivalent circuit of the unit cell.

FIGURE 2. (a) Conventional square-shaped patch and grid, (b) single rectangular patch and corresponding grid having a rectangular slot, and (c) multiple rectangular patches and corresponding grid.

waves such that their polarization is different from that of the incident waves [5]–[7]. Recently, several polarization-dependent lenses have been reported in which the thickness is about 10% of the wavelength at their operating frequency [7]–[13]. However, this thickness and the lateral dimension of the unit cell are too bulky for such lens technologies to be used in industrial applications such as 5G.

This paper describes a lens in which a tunable phase range of 180° can be achieved from a cell with a thickness of 0.548 mm (equivalent to $0.05\lambda_0$ at 28 GHz) by using new unit cell topologies combining asymmetric patches and grids. This approach is based on the discovery that the proposed multiple rectangular patch (MP) can realize lower values for in-plane capacitance. For polarization-dependent operation, we design different types of unit cells that have a nearly-zero range of variation in phase shifts for one polarized wave, but a wide range of variation for the other polarized wave. As a result, for x-polarized incident waves, the proposed lens operates as a convex lens, whereas for y-polarized incident waves, the lens operates as an FSS. Finally, measurements of fabricated samples with a relevant setup confirm the excellent performance of the proposed lens.

II. DESIGN OF POLARIZATION-DEPENDENT LENS

A. SPATIAL FILTERS EMPLOYING ASYMMETRIC TOPOLOGY

The proposed lens consists of nonperiodic unit cells operating as a spatial filter, as shown in Fig. 1. The design of the unit cells starts with an analysis of the equivalent circuits of planar patches and grids having sub-wavelength dimensions, as shown in Fig. 1(c). The equivalent circuits can be approximated by C and L [4]. The in-plane capacitance formed by the gaps between the patches of different unit cells is a function of the geometrical parameters D and s, as shown in Fig. 2(a) [14]–[17]:

$$C = \varepsilon_0 \varepsilon_{eff} \frac{2D}{\pi} \ln\left(\frac{1}{\sin\left(\frac{\pi s}{2D}\right)}\right) \qquad (1)$$
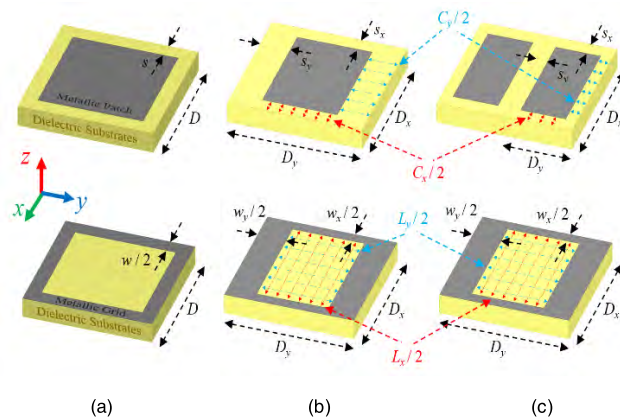
Similarly, the inductance corresponding to a grid in the unit cell is a function of D, as shown in Fig. 2(a) [14]–[17]:

$$L = \mu_0 \mu_{eff} \frac{D}{2\pi} \ln\left(\frac{1}{\sin\left(\frac{\pi w}{2D}\right)}\right) \qquad (2)$$

The T-shaped inductive network formed by $L_{substrate}$ and L_{grid} in Fig. 1(c) can be converted into an equivalent π network [14]. This converted equivalent circuit network represents a second-order bandpass filter network. High-order bandpass filter responses can be synthesized if the patch and grid patterns in the unit cell are stacked alternately. Similarly, in this study, the proposed lens is based on three metal layers, with metallic patches on the top and bottom layer and metallic grids on the middle layer. Rogers 6010 is used as the lens substrate; its permittivity, loss tangent, and thickness are 10.2, 0.0023, and 0.254 mm, respectively. Rogers 2929 Bondply is used as a bonding layer to combine the substrates; its permittivity, loss tangent, and thickness are 2.94, 0.003, and 0.04 mm, respectively.

Numerous unit cells on the proposed lens exhibit a fixed phase shift for y-polarized incident waves, but a widely tunable range of phase shifts for x-polarized incident waves. To realize different reactive responses for two orthogonally-polarized incident waves, conventional square-shaped patches and square-slotted grids are changed into rectangular-shaped patches and rectangular-slotted grids having different lengths along the x- and y-axes. In this sense, s and w in Fig. 2(a) become s_x, s_y and w_x, w_y in Fig. 2(b), while D_x and D_y, which are related to the whole size of the unit cells, are fixed to 1.8 mm. In-plane couplings between the patches are modeled as a capacitance and are a function of s_x, where s_y is fixed to 0.2 mm. Based on the assumption in (1), $s \ll D$, s_x is tuned from 0.1 mm to 1.0 mm. In this parametric sweep, the in-plane capacitance varies over a wide range of 33.91–138.32 fF for x-polarized incident waves, while the capacitance varies in a narrow range of 87.14–104.62 fF for y-polarized incident waves, as shown in Fig. 3.
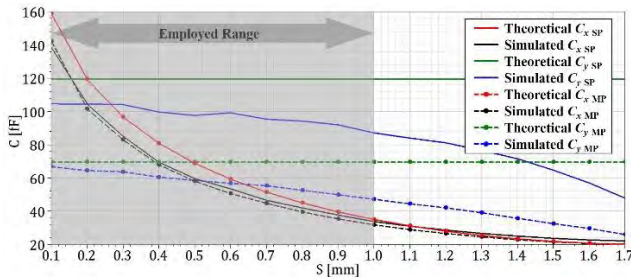
FIGURE 3. Theoretical and simulated in-plane capacitance of *x*- and *y*-polarized SP and MP.
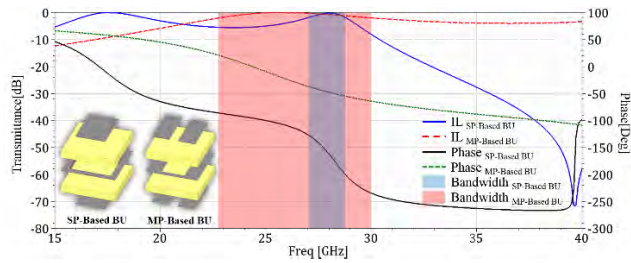
FIGURE 4. Frequency responses of the *y*-polarized bandpass unit cells based on SP unit cells and MP unit cells.

For a fixed size *D* of the unit cells, the use of MP, as shown in Fig. 2(c), can achieve a further dramatic difference between *x*-polarized and *y*-polarized responses compared to the aforementioned single rectangular patch (SP). Under the conditions mentioned in the previous paragraph, the *y*-polarized in-plane capacitance formed by the MPs varies over a narrower range of 47.32–66.87 fF, while the *x*-polarized in-plane capacitance using MPs varies over almost the same range as when utilizing SPs, enabling a wider range of polarization-dependent in-plane capacitance. Finally, bandpass unit cells (BU) are designed based on SPs and MPs, as shown in the bottom left of Fig. 4. To focus on the difference between SP- and MP-based BU designs, Fig. 4 shows the frequency responses for *y*-polarized incident waves only. As expected, the slope of the frequency response for MP-based BU is flatter than that of SP-based BU. This suggests that the utilization of MP enables a higher level of independent control of *x*-polarized BU from *y*-polarized BU. This is because, as the dimension parameters related to the *x*-polarized BU change, the frequency response of *y*-polarized BU exhibits a relatively small variation. In this sense, the insertion loss and phase shift of a 28 GHz MP-based BU example are plotted in Fig. 5 as s_x of BU is changed to 0.5, 0.6, and 0.7 mm where the IL varies less than 1 dB. As intended, the *x*-pol phase variation due to the change in s_x becomes approximately 20 degrees while the phase value corresponding to *y*-pol remains constant.

B. POLARIZATION-DEPENDENT TUNABLE RANGE OF PHASE SHIFT
This section confirms the feasibility of realizing the polarization-dependent tunable range discussed in Section II-A in a spatial filter. The lens proposed in this paper
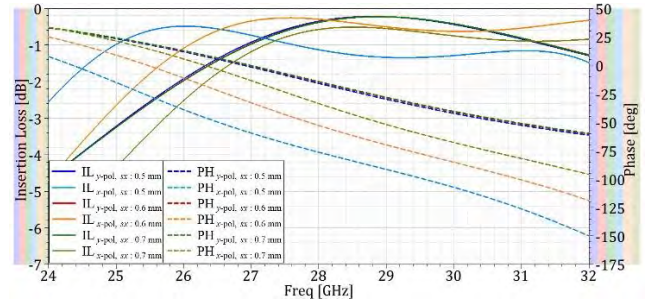
FIGURE 5. Insertion loss and phase shift of the MP-based BU as a function of s_x.
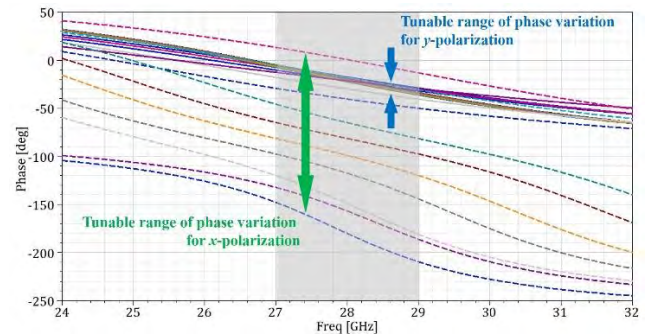
FIGURE 6. Tunable ranges of phase shift of the proposed unit cells according to *x*- and *y*-polarized incident waves.

TABLE 1. Patch and grid size, insertion loss, and phase shift of proposed unit cells.

UC#	1st Layer S_x (mm)	1st Layer S_y (mm)	2nd Layer W_x (mm)	2nd Layer W_y (mm)	3rd Layer S_x (mm)	3rd Layer S_y (mm)	*y*-pol Insertion Loss(dB)	*x*-pol Insertion Loss(dB)	*y*-pol Phase Shift (°)	*x*-pol Phase Shift (°)
1	0.9	0.4	0.4	0.6	0.9	0.4	0.097	0.938	-18.09	0.47
2	0.9	0.4	0.4	0.5	1.0	0.4	0.082	0.125	-19.00	-20.15
3	1.0	0.4	0.4	0.4	0.9	0.4	0.077	0.405	-20.17	-40.90
4	0.6	0.3	0.5	0.8	0.6	0.3	0.06	0.81	-20.40	-64.97
5	0.6	0.3	0.5	0.8	0.5	0.3	0.132	0.820	-20.88	-81.32
6	0.5	0.3	0.5	0.8	0.5	0.3	0.147	0.535	-19.72	-99.14
7	0.5	0.3	0.5	0.8	0.4	0.3	0.199	0.676	-18.04	-116.04
8	0.4	0.3	0.5	0.8	0.4	0.3	0.182	0.454	-18.58	-147.47
9	0.4	0.3	0.5	0.1	0.4	0.3	0.093	0.225	-28.18	-157.44
10	0.3	0.5	0.3	0.1	0.3	0.5	0.056	0.503	-20.41	-179.94

is intended as a transparent medium for *y*-polarized incident waves and a convex lens for *x*-polarized incident waves. Thus, all of the unit cells must provide the same level of phase shift for *y*-polarized incident waves, but they must provide significantly different levels of phase shift for *x*-polarized incident waves. Fig. 6 shows the phase shift results against the *x*- and *y*-polarized incident waves on 10 selected unit cells, and Table 1 presents the specifications of the selected unit cells. For energy-efficient beam shaping, only unit cells with an insertion loss of less than 1 dB are selected for both *x*- and *y*-polarized incident waves. When the lens is designed using the unit cells listed in Table 1, the phase shifts produced by passing *y*-polarized incident waves through the lens varies in a narrow range of approximately 10°, whereas the phase shifts for *x*-polarized incident waves can achieve a tunable range of approximately 180°.

TABLE 2. Feature comparison for previous lenses.

	Metal Layer	Thickness	Tunable Range	Note
Lens in [4]	3	$0.05\,\lambda_0$	170°	-
Lens in [18]	3	$0.05\,\lambda_0$	180°	-
Lens in [9]	3	$0.1\,\lambda_0$	210°	-
Lens in [19]	3	$0.6\,\lambda_0$	315°	With Airgap
Lens in [20]	4	$0.66\,\lambda_0$	180°	-
Lens in [21]	4	$0.175\,\lambda_0$	315°	With Airgap
Lens in [22]	4	$0.75\,\lambda_0$	360°	-
Lens in [23]	4	$0.76\,\lambda_0$	360°	-
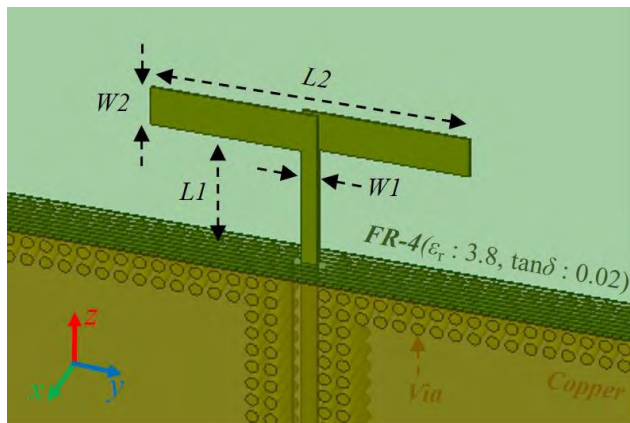
FIGURE 7. Geometry and dimension parameters of designed probe $\lambda/2$ dipole antenna.

It has been known that the increase in the number of metal and substrate layers can acquire the 360 degrees, as shown in Table 2. But this comes at the expense of practical problems such as accumulated misalignment errors among the substrates combined by numerous bonding layers and high fabrication cost, limiting the range of the commercial applications [4].

Furthermore, acquiring the tunable range was more challenged for designing dual-polarized unit cells simultaneously [9]. In this paper, the proposed lens utilizing asymmetrical multi-patches and grids have the thickness of half of the prior dual-polarized lens presented in the literature [9], but losing only 30 degrees in the tunable range of the phase shift from 210 degrees to 180 degrees.

C. PROBE DIPOLE ANTENNA DESIGN

A printed dipole antenna operating at the target frequency of 28 GHz is designed as a probe source to feed the proposed lens for full-wave simulations and measurements. The dipole source generating spherical waves is appropriate to examine the function of the proposed lens where the spherical waves are converted into the plane waves only for one polarized incident waves. Fig. 7 shows the geometry and dimension parameters of the designed dipole antenna. The designed dipole antenna was constructed using a 10-layer FR4 stack substrate, which is widely used in commercial
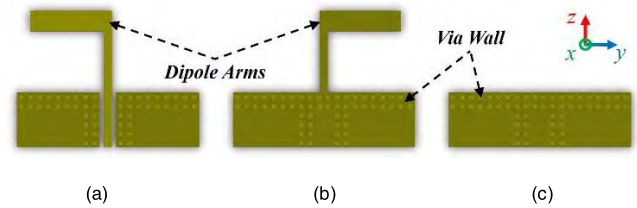
FIGURE 8. Top view of the designed probe $\lambda/2$ dipole antenna (a) 5th layer, (b) 6th layer, and (c) other layers.

millimeter-wave antenna-in-package solutions since the fabrication cost was lowered by the rapid development of 5G technology [24]–[27]. To be compatible with this printed circuit board, two arms of the dipole antenna were connected to different layers, with one connected to the 5th, signal-line layer, and the other to the 6th, ground layer, as shown in Fig. 8. Note that in the absence of other RF components for antenna design, all layers except the 5th are fully filled with copper and the layers are connected through via walls, producing a solid ground. As a result, the signal line on the 5th layer is fully surrounded by via walls, with the 4th and 6th copper layers forming a quasi-coaxial cable to minimize substrate losses at 28 GHz. As shown in Fig. 8, the via walls are added along the edge of the solid ground as a reflector. Through optimization performed by full-wave simulations, $L1$, $L2$, $W1$, and $W2$ were set to 1.5 mm, 3.8 mm, 0.2 mm, and 0.5 mm, respectively. The simulated 10-dB return loss results in a bandwidth of $\sim$ 1 GHz. Within the 1 GHz bandwidth, the antenna gain varies from 1.5–2.2 dBi and the gain is 2.0 dBi at the target frequency of 28 GHz. Note that 2.0 dBi is lower than the theoretically expected gain value, even considering the addition of the via wall reflector. This is because the dipole arms, radiating elements, and initially radiating paths are buried in FR4, a commercial and lossy substrate.

D. LENS IMPLEMENTATION USING MACRO DESIGN

This section describes the design procedure for the proposed lens using the polarization-dependent spatial filter responses discussed in Section II-B. The design steps for determine the numerous unit cell types are stated below [4], [20]:

Step 1. The antenna source, from which the proposed lens will be placed at the target distance, is first considered as per the system requirements. In this study, to observe a dramatic difference in the radiation pattern between two cases corresponding to two orthogonal polarizations of the incident waves, the probe dipole antenna designed in Section II-C was used as a quasi-spherical wave source at a target distance of 20 mm.

Step 2. The phase profiles of a propagating wave-front emitted from the probe dipole antenna are captured over a selected aperture at the selected target distance (20 mm), as shown Fig. 9. In this study, considering the size of the unit cell, the phase profiles were captured at 1.8 mm intervals on the basis of the center of each unit cell. The first quadrant of

IEEE*Access*
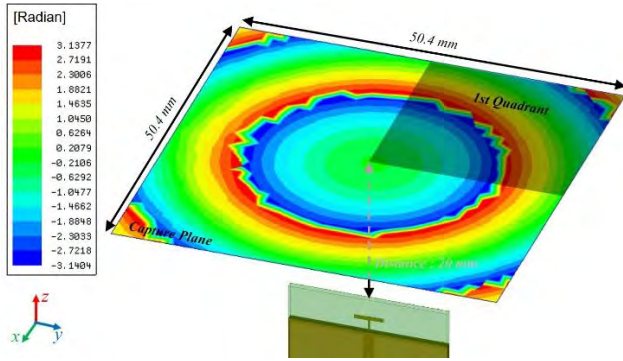
FIGURE 9. Phase distributions on captured plane at the distance of 20 mm away from the probe dipole antenna.

(a)   (b)
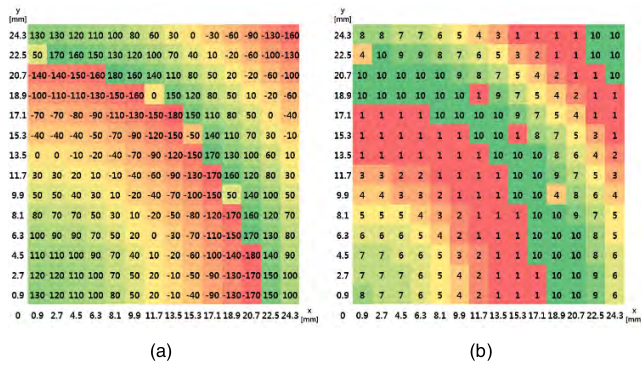
FIGURE 10. (a) First quadrant phase distributions captured at a selected distance away from the antenna and (b) distribution of the numbered unit cells selected from Table 1.
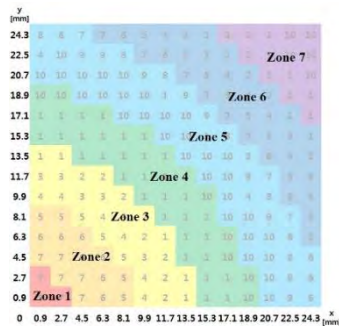
FIGURE 11. Distribution of zones selected from Fig. 11 (b).

TABLE 3. Numbered zones, incident angle, selected UC# for each zone, insertion loss and phase at the center of each zone.

Zone #	Incident theta angle in the middle of each zone (deg)	Selected UC #	phi = 0				phi = 90			
			y-pol Insertion loss of unit cell in the middle of each zone (dB)	x-pol Insertion loss of unit cell in the middle of each zone (dB)	y-pol Phase of unit cell in the middle of each zone (deg)	x-pol Phase of unit cell in the middle of each zone (deg)	y-pol Insertion loss of unit cell in the middle of each zone (dB)	x-pol Insertion loss of unit cell in the middle of each zone (dB)	y-pol Phase of unit cell in the middle of each zone (deg)	x-pol Phase of unit cell in the middle of each zone (deg)
Zone 1	0	7	0.199	0.676	-18.04	-116.04	0.199	0.676	-18.04	-116.04
		8	0.182	0.454	-18.58	-147.47	0.182	0.454	-18.58	-147.47
Zone 2	17	5	0.38	0.8	-20.03	-80.39	0.38	1	-21.29	-80.9
		6	0.39	0.67	-18.22	-98.43	0.33	0.86	-21.38	-99.52
		7	0.4	0.87	-17.04	-116.42	0.39	1.08	-18.22	-116.19
Zone 3	30	1	0.26	0.81	-16.16	-1.68	0.27	1.65	-19.13	5.68
		2	0.24	0.09	-17.08	-21.88	0.25	0.5	-20.22	-16.5
		3	0.22	0.23	-19.94	-42.17	0.25	0.39	-21.36	-41.72
		4	0.41	0.63	-16.92	-62.86	0.43	0.9	-20.27	-61.35
		5	0.44	0.6	-16.26	-78.03	0.38	1.3	-22.44	-82.28
Zone 4	41	1	0.33	0.75	-11.31	-4.25	0.3	1.02	-20.12	12.07
		10	0.18	0.36	-16.97	-175.98	0.21	0.91	-18.73	-176.82
Zone 5	48	1	0.35	0.83	-9.94	-7.53	0.32	1.28	-21.88	16.02
		4	0.49	0.68	-11.87	-64.29	0.52	0.8	-23.09	-61.23
		6	0.53	0.24	-9.36	-97.74	0.47	1.4	-24.01	-98.42
		7	0.57	0.38	-7.4	-114.26	0.53	1.42	-21.07	-112.11
		8	0.63	0.32	-6.7	-140.93	0.57	1.36	-21.41	-140.52
		9	0.27	0.18	-21.85	-155.45	0.35	1.24	-26.11	-147.97
		10	0.21	0.3	-15.32	-174.85	0.24	1.27	-19.58	-173.62
Zone 6	53	1	0.32	0.86	-4.17	-12.39	0.37	1.41	-22.91	21.37
		2	0.36	0.08	-9.56	-26.01	0.4	0.86	-22.44	-4.25
		3	0.3	0.2	-13.57	-41.27	0.38	0.64	-24.3	-39.94
		4	0.64	0.39	-6.89	-64.28	0.57	1.25	-25.35	-66.13
		5	0.61	0.38	-8.14	-77.62	0.57	1.42	-25.51	-81.96
		6	0.64	0.22	-5.51	-95.23	0.56	0.94	-24.78	-97.72
		7	0.63	0.35	-4.96	-113.6	0.56	1.46	-23.28	-111.87
Zone 7	58	1	0.35	0.62	-11.22	-15.41	0.45	1.54	-24.63	26.75
		5	0.66	0.47	-6.85	-78.18	0.65	1.57	-27.91	-82.68

the captured aperture is shown in Fig. 10(a), and the original analog phase distributions are quantized into bins of 10°, where the phase profiles are in the range −180°–180°.

Step 3. From the predetermined phase shifts, the types of unit cells at each point are selected from Table 1. In the case of y-polarized incident waves, the unit cells for all of the captured points have the same phase shift value of ~20°; in the case of x-polarized incident waves, the types of unit cells are selected to compensate different levels of phase shift in the captured points to create a flat wave-front, suggesting enhanced antenna gain toward the intended beam direction. The first quadrant of the selected unit cells is shown in Fig. 10(b).

Step 4. To utilize the effect of an incident angle of the proposed lens, the zone is formed in Fig. 11 and the calculated distance from each zone is organized as Table 3. Table 3 shows the numbered zones, incident angle, selected UC# for each zone, phase, and insertion loss at the center of each zone. From the comparisons between Table 1 and Table 3, it is assumed that variations in insertion loss and phase shift by different incident angles are not significant.

Step 5. Finally, the design of the proposed lens is completed by applying the aforementioned procedure for all four quadrants, as shown in Fig. 12.

III. FABRICATION AND MEASUREMENT

The top view of the fabricated sample of the dipole antenna is shown in Fig. 13. The fabricated 10-layer FR4 stack has a total thickness of 0.741 mm, and its dielectric constant and loss tangent are 3.8 and 0.002, respectively. Fig. 14 shows the simulated and measured return loss of the probe dipole antenna. The 10-dB return loss bandwidth of the antenna is 1.3 GHz. Fig. 15 shows a fabricated sample of the proposed polarization-dependent thin lens. It is practically useful to
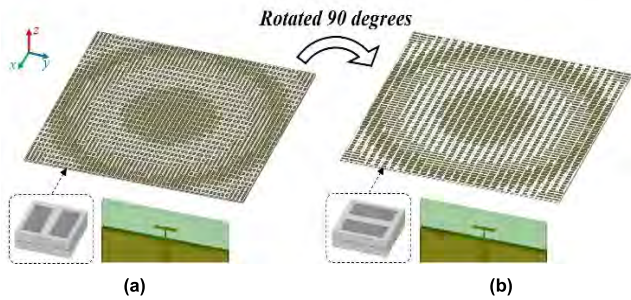
FIGURE 12. Oblique view of designed lens (a) in case of *y*-polarized incident waves and, (b) in case of *x*-polarized indent waves.

FIGURE 13. Picture of the fabricated probe dipole antenna.
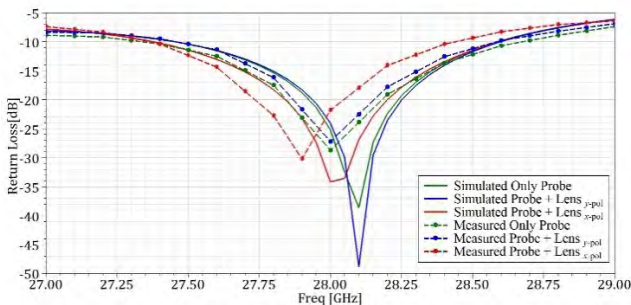
FIGURE 14. Simulated and measured return loss of the probe dipole antenna.

note that, in the fabricated sample, the existence of extra substrate areas in the exterior of the metallic lens area must be combined with a zig holder. Fig. 16 shows the simulated 3D radiation patterns corresponding to the probe dipole antenna without and with the proposed lens transforming *y*- and *x*-polarized incident waves. Fig. 16(b) shows that, for the *y*-polarized incident waves, the 3D radiation pattern formed by the waves radiating from the proposed lens is the same as the 3D radiation pattern excited using the dipole antenna without the lens. In contrast, for the *x*-polarized incident waves, the 3D radiation pattern formed by the waves radiating from the proposed lens is much sharper than the patterns in the aforementioned two cases. In each cases, the polarization purity of the proposed lens is high, indicating the low cross-pol gain compared to co-pol.

In the measurement setup, two orthogonal arrangements of the probe dipole antenna were tested to produce inci-dent waves with *x*- and *y*-polarization. Fig. 17 shows the

FIGURE 15. Top view of the fabricated MP-based lens.
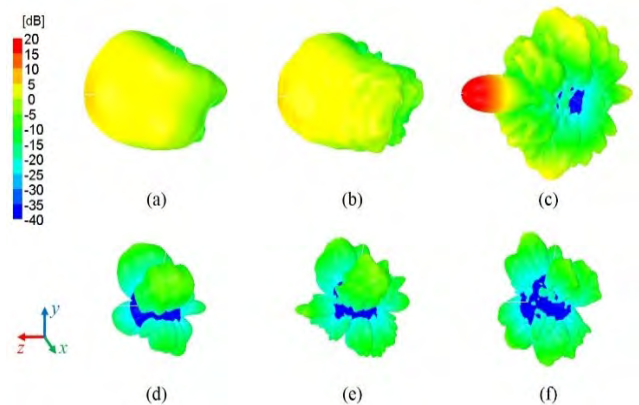
FIGURE 16. Simulated 3D radiation patterns of co-polarization corresponding to (a) only the probe dipole antenna, and the proposed lens transforming (b) *y*-polarized and (c) *x*-polarized incident waves. And simulated 3D radiation patterns of cross-polarization corresponding to (d) only the probe dipole antenna, and the proposed lens transforming (e) *y*-polarized and (f) *x*-polarized incident waves.
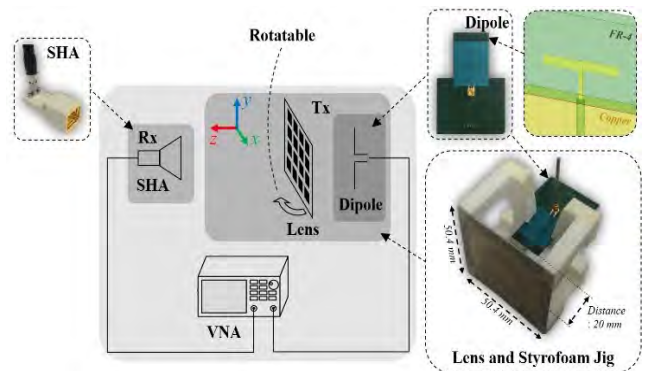
FIGURE 17. Measurement system and Styrofoam jig for the proposed lens.

measurement setup, where the proposed lens fed by the dipole antenna is used as a transmit (Tx) antenna, and a standard-gain horn antenna is used as a receive (Rx) antenna. The fabricated lens (size = 50.4 mm × 50.4 mm) was mounted on a Styrofoam jig, and the position of the $\lambda/2$ dipole antenna behind the lens was controlled to be accurately aligned with the center of the lens, maintaining the intended distance of 20 mm between the antenna and the lens.
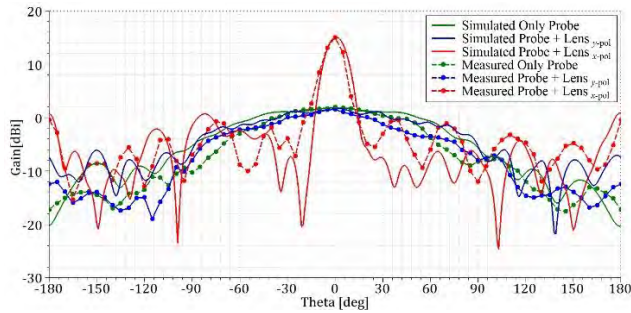
FIGURE 18. Simulated and measured radiation patterns for three different antenna configurations on the E-plane.
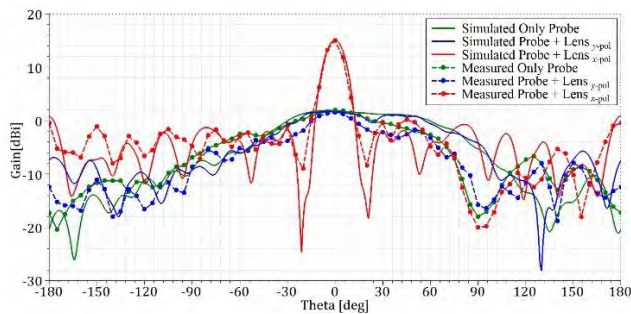
FIGURE 19. Simulated and measured radiation patterns for three different antenna configurations on the H-plane.
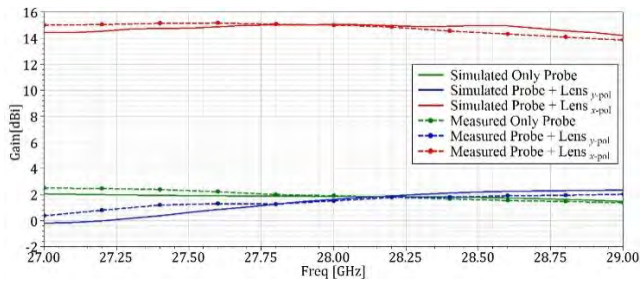
FIGURE 20. Simulated and measured gains for the cases 'Only the probe dipole antenna', 'The probe dipole antenna + the proposed lens for y-polarized incident waves' and 'The probe dipole antenna + the proposed lens for x-polarized incident waves' within 10 dB-return loss bandwidth of the dipole.

TABLE 4. Measured lens gain for distance between probe antenna and lens.

Distance between Probe Antenna and Lens	y-pol	x-pol
15 mm	2.81 dBi	14.31 dBi
17 mm	2.92 dBi	14.66 dBi
20 mm	2.64 dBi	15.06 dBi
23 mm	3.01 dBi	14.32 dBi
25 mm	2.87 dBi	14.02 dBi

Figs. 18 and 19 show the simulated and measured radiation patterns of the proposed lens on the E- and H-planes, respectively. The gain using only the probe dipole antenna was measured to be 1.9 dBi (HPBW: 95°). The proposed lens reacting to the y-polarized incident waves has a similar gain to that of the probe dipole antenna within an error

TABLE 5. Feature comparison between previous lens [9] and proposed lens.

	Previous Lens	Proposed Lens
Operation Frequency	10 GHz	28 GHz
Thickness	3.149 mm ($0.1\lambda_0$)	0.548 mm ($0.05\lambda_0$)
Number of Metal Layers	3	3
Number of Substrate Layers	2	2
Unit Cell Size	15 mm $\times$ 15 mm ($0.5\lambda_0 \times 0.5\lambda_0$)	1.8 mm $\times$ 1.8 mm ($0.168\lambda_0 \times 0.168\lambda_0$)
Tunable Range of Phase Shift	210°	180°
Lens Size	300 mm $\times$ 300 mm ($10\lambda_0 \times 10\lambda_0$)	50.4 mm $\times$ 50.4 mm ($4.71\lambda_0 \times 4.71\lambda_0$)
Distance from the Feed Antenna	215 mm ($21.5\lambda_0$)	20 mm ($1.87\lambda_0$)
Bandwidth	1.75 GHz	1 GHz
Gain Enhancement Factor (Lens Gain)	16.5 dB	13 dB

range of 0.5 dB. However, the proposed lens reacting to the x-polarized incident waves exhibits a significant gain improvement of 13 dB compared to the reference probe dipole, and thus the corresponding radiation pattern is shaped to have a narrow beam with HPBW of approximately 11°. Note that the use of a quasi-omnidirectional dipole might cause undesired scattering on mechanical fixtures, leading to slight discrepancies between the simulated and measured results. The gains corresponding to the cases of the probe dipole antenna without and with the proposed lens were simulated and measured in the range of the probe dipole antenna bandwidth, as shown in Fig. 20. This confirms that there is good agreement between the simulated and measured results, as well as a stable gain bandwidth in the given range. In this study, aperture efficiency for x-polarized incident waves is calculated as low as 14.7%. This is because a printed dipole antenna rather than a directive horn antenna is used as a spherical-wave source which is more appropriate to demonstrate the proposed dual polarized operation showing two extreme cases of broad and narrow beams. Table 4 shows the gain variation due to the change in the distance between the probe antenna and the lens. In the case of x-pol, the maximum gain enhancement is achieved at the desired distance of 20 mm.

Finally, Table 5 compares the features of a previous lens [9] with those of the proposed lens. The thickness of the proposed lens has been significantly reduced from $0.1\lambda_0$ to $0.05\lambda_0$ at the expense of a slight reduction in the tunable range of phase shift from 210° to 180°. The gain enhancement factor of the proposed lens (lens gain) is 3.5 dB lower than that of the prior lens because the lens size and distance from the feed antenna are much smaller for the proposed lens than for the previous lens, which affects the total antenna volume.

IV. CONCLUSION

This paper has presented a novel millimeter-wave thin lens exhibiting different beam shaping properties according to the

polarization of the incident waves. When x-polarized waves are incident on the proposed lens, the radiation pattern of the waves radiating from the lens is much narrower than that of the probe $\lambda/2$ dipole antenna, functioning as a convex lens.

In contrast, for the y-polarized incident waves, the radiation pattern of the waves radiating from the lens is almost the same as that of the probe dipole, functioning as a transparent medium. A novel combination of the proposed MPs and asymmetric grids can achieve a tunable phase range of $180°$. This enables the lens thickness to be as little as $0.05\lambda_0 (= 0.548$ mm) at 28 GHz.

REFERENCES

[1] M. Hussein, J. Zhou, Y. Huang, and B. Al-Juboori, "A low-profile miniaturized second-order bandpass frequency selective surface," *IEEE Antennas Wireless Propag. Lett.*, vol. 16, pp. 2791–2794, 2017.

[2] E. Kim, S. T. Ko, Y. J. Lee, and J. Oh, "Millimeter-wave tiny lens antenna employing U-shaped filter arrays for 5G," *IEEE Antennas Wireless Propag. Lett.*, vol. 17, no. 5, pp. 845–848, May 2018.

[3] N. Behdad, "Miniaturized-element frequency selective surfaces (MEFSS) using sub-wavelength periodic structures," in *Proc. IEEE Radio Wireless Symp.*, Orlando, FL, USA, Jan. 2008, pp. 347–350.

[4] J. Oh, "Millimeter-wave thin lens employing mixed-order elliptic filter arrays," *IEEE Trans. Antennas Propag.*, vol. 64, no. 7, pp. 3222–3227, Jul. 2016.

[5] S. Handa, R. Kuse, T. Hori, and M. Fujimoto, "Spatial filter by using multilayered FSS for orthogonal polarization conversion," in *Proc. Asia–Pacific Radio Sci. Conf. (URSI AP-RASC)*, Seoul, South Korea Aug. 2016, pp. 1416–1417.

[6] C. Pfeiffer and A. Grbic, "Millimeter-wave transmitarrays for wavefront and polarization control," *IEEE Trans. Microw. Theory Techn.*, vol. 61, no. 12, pp. 4407–4417, Dec. 2013.

[7] J. M. Kovitz, Y. Rahmat-Samii, and J. Choi, "Dispersion engineered right/left-handed transmission lines enabling near-octave bandwidths for wideband CP patch arrays," in *Proc. IEEE Int. Symp. Antennas Propag. USNC/URSI Nat. Radio Sci. Meeting*, Jul. 2015, pp. 2525–2526.

[8] E. G. Plaza, G. León, S. Loredo, and F. Las-Heras, "Dual polarized transmitarray lens," in *Proc. 8th Eur. Conf. Antennas Propag. (EuCAP)*, The Hague, The Netherlands, Apr. 2014, pp. 2305–2308.

[9] K. Pham *et al.*, "Design of wideband dual linearly polarized transmitarray antennas," *IEEE Trans. Antennas Propag.*, vol. 64, no. 5, pp. 2022–2026, May 2016.

[10] K. T. Pham, R. Sauleau, E. Fourn, F. Diaby, A. Clemente, and L. Dussopt, "Dual-band transmitarrays with dual-linear polarization at ka-band," *IEEE Trans. Antennas Propag.*, vol. 65, no. 12, pp. 7009–7018, Dec. 2017.

[11] K. Pham, N. Nguyen, L. Le Coq, R. Sauleau, A. Clemente, and L. Dussopt, "Experimental characterization of dual linearly polarized transmitarray antennas at X-band," in *Proc. 11th Eur. Conf. Antennas Propag. (EUCAP)*, Mar. 2017, pp. 2387–2391.

[12] H. Wang, Z. Wang, Z. Wu, and Y. Zhang, "Dual-polarized lens antenna based on multimode metasurfaces," in *Proc. IEEE Asia–Pacific Conf. Antennas Propag. (APCAP)*, Auckland, New Zealand Aug. 2018, pp. 521–523.

[13] Y. Zuo, Z. Shen, and Y. Feng, "Dual-band and dual-polarized bandpass frequency selective structure," in *Proc. Asia–Pacific Microw. Conf.*, Melbourne, VIC, USA, Dec. 2011, pp. 769–772.

[14] M. Al-Joumayly and N. Behdad, "A generalized method for synthesizing low-profile, band-pass frequency selective surfaces with non-resonant constituting elements," *IEEE Trans. Antennas Propag.*, vol. 58, no. 12, pp. 4033–4041, Dec. 2010.

[15] N. Behdad and M. Al-Joumayly, "A Generalized synthesis procedure for low-profile, frequency selective surfaces with odd-order bandpass responses," *IEEE Trans. Antennas Propag.*, vol. 58, no. 7, pp. 2460–2464, Jul. 2010.

[16] O. Luukkonen *et al.*, "Simple and accurate analytical model of planar grids and high-impedance surfaces comprising metal strips or patches," *IEEE Trans. Antennas Propag.*, vol. 56, no. 6, pp. 1624–1632, Jun. 2008.

[17] S. A. Tretyakov, *Analytical Modeling in Applied Electromagnetics*. Norwood, MA, USA: Artech House, 2003.

[18] K. K. Katarea, A. Biswas, and M. J. Akhtar, "Microwave beam steering of planar antennas by hybrid phase gradient metasurface structure under spherical wave illumination," *J. Appl. Phys.*, vol. 122, no. 23, 2017, Art. no. 234901.

[19] C. Tian, Y.-C. Jiao, G. Zhao, and H. Wang, "A wideband transmitarray using triple-layer elements combined with cross slots and double square rings," *IEEE Antennas Wireless Propag. Lett.*, vol. 16, pp. 1561–1564, 2017.

[20] M. A. Al-Joumayly and N. Behdad, "Wideband planar microwave lenses using sub-wavelength spatial phase shifters," *IEEE Trans. Antennas Propag.*, vol. 59, no. 12, pp. 4542–4552, Dec. 2011.

[21] T. Nguyen, B. D. Nguyen, V.-S. Tran, M. Linh, and L. H. Trinh, "Wideband unit-cell for linearly polarized X-band transmitarray applications," in *Proc. Int. Conf. Adv. Technol. Commun. (ATC)*, Oct. 2018, pp. 125–128.

[22] B. Xi, Q. Xue, L. Bi, and Y. Wang, "Design of multi-beam transmitarray antenna using alternating projection method," in *Proc. IEEE Int. Conf. Comput. Electromagn. (ICCEM)*, Chengdu, China, Mar. 2018, pp. 1–3.

[23] A. H. Abdelrahman, P. Nayeri, A. Z. Elsherbeni, and F. Yang, "Bandwidth improvement methods of transmitarray antennas," *IEEE Trans. Antennas Propag.*, vol. 63, no. 7, pp. 2946–2954, Jul. 2015.

[24] W. Hong, S.-T. Ko, Y. Lee, and K. H. Baek, "Compact 28 GHz antenna array with full polarization flexibility under yaw, pitch, roll motions," in *Proc. 9th Eur. Conf. Antennas Propag. (EuCAP)*, Lisbon, Portugal, Apr. 2015, pp. 1–3.

[25] W. Hong, S. Ko, Y. Lee, and K. H. Baek, "Multi-polarized antenna array configuration for mmWave 5G mobile terminals," in *Proc. Int. Workshop Antenna Technol. (iWAT)*, Seoul, South Korea, Mar. 2015, pp. 60–61.

[26] K. H. Baek and W. Hong, "Highly miniaturized vertical end-fire antenna array for mmWave wireless communication," in *Proc. IEEE Antennas Propag. Soc. Int. Symp. (APSURSI)*, Orlando, FL, USA, Jul. 2013, pp. 992–993.

[27] G. S. Karthikeya, M. P. Abegaonkar, and S. K. Koul, "Low cost high gain triple band mmWave Sierpinski antenna loaded with uniplanar EBG for 5G applications," in *Proc. IEEE Int. Conf. Antenna Innov. Mod. Technol. Ground, Aircr. Satell. Appl. (iAIM)*, Bangalore, India, Nov. 2017, pp. 1–5.

INSEOP YOON received the B.S. degree in electronic engineering from Korea Polytechnic University, South Korea, in 2011, and the M.S. degree in electronic engineering from Inha University, South Korea, in 2013, where he is currently pursuing the Ph.D. degree.

His current research interests include antenna design for 5G telecommunications and millimeter-wave radar systems.

JUNGSUEK OH (S'08–SM'17) received the B.S. and M.S. degrees from Seoul National University, South Korea, in 2002 and 2007, respectively, and the Ph.D. degree from the University of Michigan at Ann Arbor, in 2012.

From 2007 to 2008, he was a Hardware Research Engineer with Korea Telecom, where he was involved in the development of flexible RF devices. In 2012, he joined the Radiation Laboratory, University of Michigan, as a Postdoctoral Research Fellow. From 2013 to 2014, he was a Staff RF Engineer with Samsung Research America, Dallas, where he focused on the 5G/millimeter-wave antenna systems as a Project Leader. From 2015 to 2018, he was a Faculty Member with the Department of Electronic Engineering, Inha University, South Korea. He is currently an Assistant Professor with the School of Electrical and Computer Engineering, Seoul National University, South Korea. He has published more than 40 technical journal and conference papers. His research areas include millimeter-wave beam focusing/shaping techniques, antenna miniaturization for integrated systems, and radio propagation modeling for indoor scenarios. He has served as a TPC Member and as a Session Chair for the IEEE AP-S/USNC-URSI and ISAP. He received the 2011 Rackham Predoctoral Fellowship Award from the University of Michigan. He has served as a Technical Reviewer for the IEEE TRANSACTIONS ON ANTENNAS AND PROPAGATION and IEEE ANTENNA AND WIRELESS PROPAGATION LETTERS.

● ● ●